Title
Indium Tin-Doped Oxide Interactions with Solvent Radiolysis Products

Journal
The Journal of Physical Chemistry C, 129(47)

ISSN
1932-7447

Authors
McLachlan, Jeffrey R
Hou, Xiangyang
Ortega, Gabriela
et al.

Publication Date
2025-11-27

DOI
10.1021/acs.jpcc.5c05312

Indium Tin-Doped Oxide Interactions with Solvent Radiolysis Products

Jeffrey R. McLachlan,[a,b,c] Xiangyang Hou,[a,d] Gabriela Ortega,[a] Gregory P. Horne,*[e] Christopher J. Dares*[a]

[a] Department of Chemistry and Biochemistry, Florida International University, Miami, Florida 33199, United States

[b] Chemical Sciences Division, Lawrence Berkeley National Laboratory, Berkeley, California 94720, United States

[c] Department of Nuclear Engineering, University of California, Berkeley, California 94720, United States

[d] Department of Chemistry, University of Utah, Salt Lake City, Utah 84112, United States

[e] Center for Radiation Chemistry Research, Idaho National Laboratory, PO Box 1625, Idaho Falls, Idaho 83415, United States

Corresponding author emails: cdares@fiu.edu and gregory.holmbeck@inl.gov

Abstract

Transparent conductive oxides (TCOs), such as indium tin-doped oxide (ITO), are ubiquitous as components of electronics and are ideal electrode substrates for catalysis, energy transformation reactions, and energy storage applications. Recently, researchers have recognized their effectiveness as electrode materials for manipulating actinide oxidation states in solution. Despite their popularity as electrode materials, prior studies focused extensively on the direct radiolysis of TCO materials in air and rarely examined these effects within a solution, limiting our fundamental understanding of the interactions between solvent radiolysis products and these substrates in high radiation environments. Here we characterize the effects of solvent radiolysis products—arising from the gamma irradiation of water, aqueous nitric acid solutions, and *n*-dodecane—on the composition, surface speciation, and band structure of ITO thin films on a glass substrate as a function of absorbed dose using UV-visible spectroscopy, scanning electron microscopy, photoelectrochemistry, and X-ray photoelectron spectroscopy. Our work demonstrates that mesoporous thin film electrodes of ITO exposed to gamma radiation in each solvent accumulate defects and exhibit solvent and dose dependent changes to their surface and interfacial properties. These electrodes maintain their electrochemical function and improve their photoelectrochemical performance up to at least 100 kGy of accumulated gamma dose, confirming their utility in solvents exposed to ionizing radiation fields.

1. Introduction

Transparent conducting oxides (TCOs) comprise a group of wide bandgap semiconductors characterized by their high conductivity and optical transparency in the visible region. Their microstructure and interfacial characteristics are readily altered to provide increased surface area and reaction selectivity by varying TCO deposition methods[1] and through ligand surface modifications,[2] respectively. These characteristics have led to the development and use of bare TCOs and ligand-modified TCOs in many applications, including optoelectronics,[3] sensors, photocatalysis,[4] solar cells,[5] and material sciences.[6]

Electronics that utilize TCO components are used in spacecraft and nuclear facilities. These environments expose the TCO materials to ionizing radiation fields. Hence, prior studies focused on the direct effect of gamma radiation on TCO materials in air, examining changes in their optical, physical, and electrical properties. Typical trends observed in relation to increasing absorbed gamma dose include decreased resistivity,[7,8] optical transmittance,[1,7–10] and optical bandgap;[1,7,10] increased lattice defects (e.g., oxygen vacancies, f-centers, interstitial hydrogen); and variations in grain size,[1,7,9] crystallinity,

orientation,[1,7] surface roughness, and surface area.[7,9] The aggregate effects of these radiation-induced changes in air often result in diminished physical, chemical, optical, and electrical TCO properties, although improvements in their overall performance have also been reported.[11]

Recently, the oxidation state distributions of *f*-elements, including Ce,[12,13] Eu,[12] U,[14] and Am,[15,16] have been manipulated electrochemically and photoelectrochemically[4] in aqueous 0.1–3.0 M nitric acid (HNO_3) solutions using ligand-modified and non-derivatized mesoporous indium tin-doped oxide (nITO) electrodes. In these experiments, the TCO materials were submerged in a solvent matrix that, in the presence of the actinide elements (U and Am), was also subjected to an inherent ionizing radiation field. Consequently, indirect radiation effects—those arising from the interaction of TCO materials with solvent radiolysis products—may play a significant role in the performance and longevity of these materials, in addition to the previously investigated direct radiation effects—those arising from the direct deposition of ionizing radiation energy into the electrons of the TCO materials.

Solvents of interest here pertain to those employed by used nuclear fuel (UNF) hydroreprocessing solvent systems—i.e., water, HNO_3, and *n*-dodecane. The interaction of gamma radiation with each of these solvents results in the formation of solvated electrons (e_s^-) and various reactive radical, ionic, and molecular species. Water radiolysis products include the hydrated electron (e_{aq}^-), the hydrogen atom ($H^\bullet$), molecular hydrogen gas (H_2), hydrogen peroxide (H_2O_2), and the hydroxyl radical ($^\bullet OH$):[17]

$$H_2O \rightsquigarrow e_{aq}^-, {}^\bullet OH, H^\bullet, H_2, H_2O_2, H_{aq}^+, \quad (1)$$

where $H^\bullet$, $^\bullet OH$, and H_2O_2 play a significant role in radiation-induced redox processes in acidic aqueous solutions. The radiolysis products arising from the irradiation of HNO_3 include those from water (Reaction 1), in addition to the nitrate radical ($^\bullet NO_3$) and nitrous acid (HNO_2):[17–19]

$$NO_3^- + e_{aq}^-/H^\bullet \rightarrow\rightarrow HNO_2, \quad (2)$$

$$HNO_3 + {}^\bullet OH \rightarrow NO_3^\bullet + H_2O, \quad (3)$$

$$HNO_3 \rightsquigarrow e_{aq}^-, NO_3^\bullet, HNO_2, {}^\bullet O^\bullet, H_{aq}^+. \quad (4)$$

Lastly, *n*-dodecane radiolysis products include e_S^-, various alkane radicals ($R\text{-}CH_2^\bullet$), radical cations ($R\text{-}CH_3^{\bullet+}$), and $H^\bullet$:[17,20]

$$R\text{-}CH_3 \rightsquigarrow e^-, R\text{-}CH_3^{\bullet+}, R\text{-}CH_2^\bullet, {}^\bullet CH_3, H^\bullet, H_2. \quad (5)$$

In all three media, the redox-active radiolysis products that form have the capacity to react with TCO materials, thereby promoting indirect radiation effects. To date, these indirect radiation effects on the physical, chemical, optical, and electrical properties of TCO materials, with respect to electro- and photoelectrocatalysis, have not been examined.

Therefore, because TCO materials are increasingly being incorporated into the fundamental and applied study of actinide elements, it is of utmost importance to examine the effects of indirect radiolysis on the physical and chemical properties of TCO materials. Herein, we examine the effect of gamma radiation on nITO electrodes in contact with air and submerged in water, aqueous 0.1 M HNO_3, and *n*-dodecane solutions. This study includes an examination of changes in nITO: *(i)* microstructure using scanning electron microscopy (SEM); *(ii)* film elemental composition and speciation using X-ray photoelectron spectroscopy (XPS); *(iii)* optical properties using UV-visible (UV-vis) spectroscopy and Tauc analysis; and *(iv)* flat band potential using the Gärtner–Butler method. Finally, the electrochemical and photoelectrochemical performance of gamma-irradiated nITO electrodes were assessed via the electrochemical response of ferrocene in solution and the photoelectrochemical oxidation of H_2O_2, respectively.

2. Experimental Section

Materials

All chemicals were purchased from Fisher Scientific and used as received. Graphite rod and saturated calomel reference electrodes were purchased from CH Instruments. Sheets of Tec 15 FTO Glass were purchased from Hartford Glass, Co. Indium tin oxide nanoparticle dispersion in ethanol (In_2O_3:SnO_2 = 95:5, 18 nm, 20 wt%; Stock#US7658) was purchased from US Research Nanomaterials, Inc. The preparation of nITO electrodes is described elsewhere.[44]

Gamma Irradiations

The static irradiation of nITO electrodes in air, 18.2 MΩ water, aqueous 0.1 M HNO_3 (≥99.999 % trace metals basis), and *n*-dodecane (≥99 % anhydrous) was achieved using the Idaho National Laboratory (INL) Center for Radiation Chemistry Research (CR2) Foss Therapy Services Model 812 Cobalt-60 Irradiator. The nITO samples were placed in 20 mL screw-cap vials and completely submerged in 15 mL of a given solvent. The sealed vials were then irradiated under "deaerated" conditions. Sealed vials were considered deaerated upon exposure to relatively low absorbed gamma doses due to the radiolytic consumption of dissolved oxygen. In the absence of agitation, the rate of headspace gas transfer into the liquid phase is slow compared to the radiolytic loss of O_2.[45] Gamma irradiations were performed in triplicate at ~40 °C, as determined by a thermocouple. Doses of up to 133.3 kGy were attained using dose rates ranging from 40 to 440 Gy min^{-1}, as determined by Fricke dosimetry.[17,46] Dose rates were subsequently corrected for sample position, radioactive decay (Co-60, $t_{1/2}$ = 5.27 years, $E_{\gamma 1}$ = 1.17 MeV, and $E_{\gamma 2}$ =1.33 MeV), and the mass energy-absorption coefficient ratio between *n*-dodecane and water (1.04). Dose rates reported for samples irradiated in air correspond to those determined by Fricke dosimetry. Electrodes soaked or irradiated in aqueous solvents were removed from solution after 5 hours and 20 minutes, while electrodes soaked or irradiated in *n*-dodecane were removed from solution after 6 hours. Electrodes were rinsed with methanol and allowed to dry in air prior to subsequent analysis.

Surface Characterization

SEM images were acquired on a Hitachi S-4700 Cold Cathode Field Emission Scanning Electron Microscope. X-ray photoelectron spectra were collected with a Kratos Axis Ultra DLD X-ray Photoelectron Spectrometer using a monochromatic Al K-alpha source (1486.6 eV). Conductive ITO samples were ground to the spectrometer using copper tape to mitigate charging effects. The reported energies were corrected by setting the lowest binding energy component of the C 1s peak to 284.6 eV. Additional details describing the methods used to peak fit high-resolution In 3d and Sn 3d spectra are given in section "*XPS of nITO electrodes*" in the text. Pore size analysis was performed using ImageJ software.

ICP-MS

The quantity of Sn and In leached from nITO electrodes into 18.2 MΩ water or aqueous 0.1 M HNO_3 solutions after soaking (0 kGy) or exposure to gamma radiation (100 kGy) were determined using ICP-MS. Each solvent-dose combination was analyzed in triplicate. An Agilent 7900 ICP-MS was used to perform liquid sample analysis of four solvent (water or aqueous 0.1 M HNO_3) and irradiation (0 or 100 kGy) pairings. Three separate electrode exposures were performed for each condition pairing and were each analyzed for Sn and In. An additional element (Rh) was monitored as an internal standard at 100 ppb. Control samples were analyzed to determine sample contamination or carryover (method blanks), reference standard contamination (continuing calibration blank), instrument drift (continuing calibration verification), and matrix effect issues (Sn/In spiked samples).

Spectroscopic Experiments

UV-vis spectra were acquired on an Agilent Technologies Cary 6000i. Electrodes were held perpendicular to the spectrometer's incident light path with the conductive side of the electrode facing the incident light source. The direct optical band gap (E_g) was estimated using the Tauc method for a direct electron transition, which is described in detail elsewhere.[47–49] Briefly, absorbance data (**Figure S1**) were used to calculate the absorption coefficient (α) using the relationship $\alpha = (\ln(10) \times \text{Abs})/L$, where *L* is the film thickness. An average nITO film thickness of 35 ± 2 μm was determined from SEM images of each

soaked (0 kGy) or irradiated (100 or 133.3 kGy) electrode's profile view. The photon energy was converted from wavelength (nm) to *hv* (eV) using the relationship $hv = 1239.8/\lambda$. Finally, the absorption coefficients and photon energies were used to plot $(\alpha hv)^2$ versus *hv* (Tauc plot) (**Figure S10**). For simple semiconductors that do not contain components that absorb at energies lower than the band gap, an extrapolation of the linear region of the plot to $(\alpha hv)^2 = 0$ yields the estimated direct optical band gap value. For samples that are convoluted by species that absorb at energies lower than the band gap, an extrapolation of the linear region of the plot to its intersection with the extrapolated baseline yields the estimated direct optical band gap.

Electrochemical and Photoelectrochemical Experiments

Electrochemical methods were performed using a three-electrode setup with either a CH Instruments CHI650E potentiostat or a BioLogic SP-300 potentiostat. A nITO electrode was used as the working electrode, a graphite rod was the counter electrode, and either an SCE (aqueous) or a silver/silver chloride wire (non-aqueous) was the reference electrode. Electrochemical experiments were conducted in an acetonitrile solution containing 1 mM ferrocene analyte and 0.1 M tetrabutylammonium hexafluorophosphate electrolyte. A Thorlabs M375L4 mounted LED was used to illuminate the nITO working electrode for photoelectrochemical experiments. The illumination power density at 375 nm was measured using a ThorLabs PM400K5. A Gärtner–Butler analysis was conducted in a solution of aqueous 0.1 M HNO_3 containing 0.5 M H_2O_2 and performed at three different illumination intensities (70, 100, and 120 mW/cm^2). The observed electrochemical and photocurrents were normalized as current density using the 2D surface area of the nITO working electrodes.

3. Results and Discussion

3.1. Characterization

3.1.1. UV-vis Spectroscopy of nITO Electrodes

The visible region optical transparency of nITO materials present a major advantage over the use of opaque electrode materials such as platinum, gold, or carbon, permitting the use of optical characterization techniques through the conductive substrate. Unfortunately, the direct radiolysis of condensed phase materials leads to darkening over time due to the accumulation of lattice defects and colored f-centers. The effect of solvent radiolysis products on the darkening process was assessed as a function of accumulated gamma dose in air, H_2O, aqueous 0.1 M HNO_3, and *n*-dodecane. The as-prepared nITO electrodes were characterized by a yellow strip of mesoporous ITO doctor-bladed on top of a planar transparent fluorine-doped tin oxide (FTO)-coated glass substrate (12-15 Ω/sq). After exposure to Co-60 gamma radiation, the FTO coated glass substrate turned dark brown and the ITO film turned blue (**Figure 1** ***inset***). This behavior is consistent with the radiation-induced formation of defects, such f-centers, in these materials.[1] Additionally, the color of ITO films changes from yellow to blue/grey when annealed in a reducing atmosphere, such as H_2 gas,[21] or when produced from solvothermal processes where the organic solvent serves as a reductant.[22] The blue/grey ITO produced through these processes exhibit increased carrier concentration and conductivity. This enhancement is often attributed to the materials reduction coinciding with the formation of defects such as oxygen vacancies, f-centers, and interstitial hydrogen atoms that interact with lattice oxygen atoms to form hydroxyl groups.[22,23] It is likely that gamma irradiation of ITO substrates cause similar effects. UV-vis spectra of a series of soaked and irradiated (0–100 kGy) nITO electrodes submerged in aqueous 0.1 M HNO_3 solution are shown in **Figure 1**. There is a dose-dependent increase in the visible region (400–800 nm) of the irradiated nITO film (**Table S1** of the Supplementary Information, SI) with the largest change occurring within the first 25 kGy of absorbed dose. Similar observations were made for all conditions examined here (**Figure S1** and **Figure S2**), indicating that the direct deposition of energy from gamma radiation is the primary factor causing electrode darkening, while interactions with solvent radiolysis products have only a minor effect on the absorbance spectra of nITO

materials. Furthermore, these findings suggest that the use of optical techniques through the nITO substrate may prove challenging at higher absorbed doses (≥ 25 kGy).

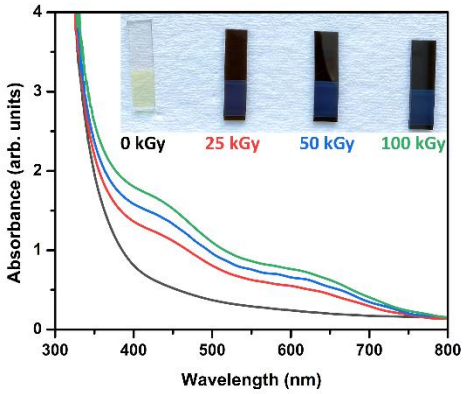

Figure 1. UV-vis spectra of nITO electrodes after exposure to 0 (**black**), 25 (**red**), 50 (**blue**), and 100 (**green**) kGy gamma radiation in an aqueous 0.1 M HNO_3 solution, wherein the electrodes were submerged for a total of 320 minutes. *Inset:* nITO electrodes exposed to (from left to right) 0, 25, 50, and 100 kGy gamma radiation in an aqueous 0.1 M HNO_3 solution. The transparent/brown section of the electrode corresponds to the underlying FTO coated glass substrate. The yellow/blue section of the electrode corresponds to the thin nITO film. The FTO coated glass substrate was used as a blank to record the change in the UV-vis spectrum of only the nITO component of the electrode.

3.1.2. SEM of nITO Electrodes

Morphological changes of condensed phase matter can alter the material's properties, such as increasing charge recombination rates and lowering the electroactive surface area. The underlying mechanisms that describe how the size of pores change in porous materials with exposure to ionizing radiation have not been fully identified in metal oxide materials. In other porous oxide materials, like mesoporous silica for instance, atomic displacements, changes in grain size, and phase changes have been some effects associated with shifts in pore size distributions.[24–26] Notably, one study examined the effect the presence of water had on the pore size of mesoporous silica irradiated with heavy ions.[24] In this study they showed that in the absence of water, pores shrank or collapsed with exposure to radiation, while those containing water shrank to a much lesser extent. This suggests that solvents and their radiolysis products likely have a significant impact on the evolution of porous material morphologies within a radiation field.

Changes in the microstructure of nITO samples soaked (0 kGy) or irradiated (100 kGy for air, water, and aqueous 0.1 M HNO_3 and 133.3 kGy for *n*-dodecane) in each solvent were examined by SEM (**Figure 2**). Pore size distribution and average pore size measurements (**Figure S3**, T**able S2**) were determined using ImageJ software. Soaking and exposure to gamma radiation in all solvents lead to statistically insignificant changes in the average pore size observed at the surface of nITO electrodes. However, the pore size distribution was different as a function of solution type and absorbed dose in some instances. For example, electrodes soaked in each solution had a lower distribution of very small pores (≤ 0.4 nm^2) compared to pristine electrodes. Electrodes irradiated in air and *n*-dodecane exhibited very minor changes in pore size distribution compared to their soaked counterparts. Electrodes irradiated in water and 0.1 M HNO_3 had an increased distribution of small pores (≤ 0.6 nm^2) that coincided with a decreased distribution in mid-sized pores (0.6 nm$^2 \leq x \leq 3.0$ nm^2). This suggests that water and nitrate radiolysis products promote the creation of small pores while combining mid-size pores into fewer large pores. Interestingly, gamma irradiation in air, water, and 0.1 M HNO_3 caused large pores to form (≥ 4.0 nm^2), while electrodes irradiated in *n*-dodecane did not exhibit this behavior. At this time, the mechanisms governing these observed behaviors is unclear. However, it can be deduced that solvent radiolysis products do play an intricate role in controlling the microsctructure of porous metal oxide materials subjected to gamma radiation.

.

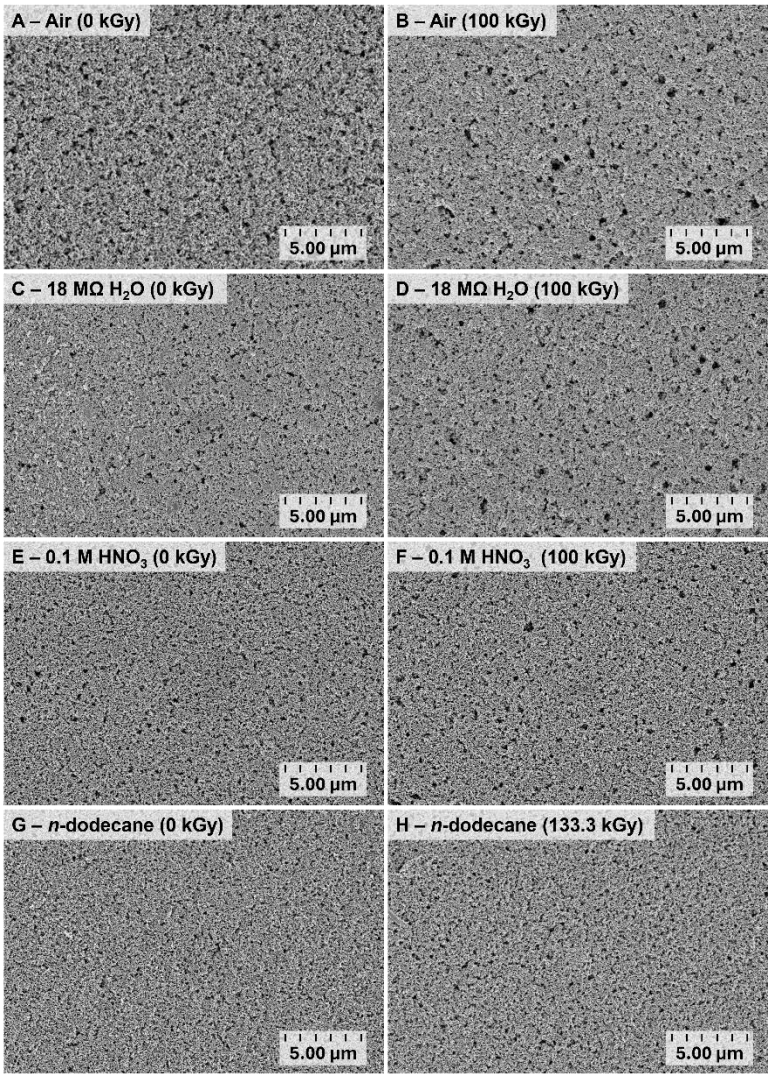

Figure 2. SEM images of the surface of nITO electrodes after exposure to air **(A)** or soaking in H_2O **(C)**, aqueous 0.1 M HNO_3 **(E)**, and *n*-dodecane **(G)** solutions, or after being exposed to gamma radiation (100 kGy or 133.3 kGy to solvent) in air **(B)** or submerged in H_2O **(D)**, aqueous 0.1 M HNO_3 **(F)**, and *n*-dodecane **(H)** solutions.

3.1.3. XPS of nITO Electrodes

The composition and speciation of elements at an electrode's interface dictate its electrochemical and photochemical properties. This includes the states that make up the material's valence and conduction band, as well as sites that may be required for specific electrocatalytic pathways. As both direct and indirect radiation effects can alter the surface of nITO materials, XPS was utilized to monitor changes in the relative atomic concentration and local atomic environment of In, Sn, O, and C elements as a function of absorbed gamma dose and solvent type (**Table *1***). Based upon these observed changes and knowledge of the solvent radiolysis species generated, mechanistic information on their interaction with nITO materials may be postulated. It is important to note that because these nITO electrodes were irradiated in air or in a solvent, any transiently generated reactive surface sites, such as oxygen vacancies, will have been passivated prior to these *ex-situ* measurements.[27,28]

Table 1: Relative atomic concentration % of designated elements determined from XPS quantification.

Solvent	Dose (kGy)	Element					Ratio		
		Sn[a]	In[b]	O[c]	C[d]	N[e]	M:O[f]	In_2O_3:$In(OH)_3$	SnO_2:$Sn(OH)_x$
Air	0	6.0	31.6	51.1	11.3	-	42:58	58:42	49:51
	100	6.1	28.5	48.8	16.7	-	41:59	62:38	47:53
H_2O	0	5.9	29.4	48.8	15.9	-	42:58	61:39	47:53
	100	5.8	29.4	48.7	16.1	-	42:58	61:39	50:50
HNO_3	0	6.0	28.9	48.3	16.3	0.4	42:58	63:37	50:50
	100	6.4	29.4	49.1	14.6	0.4	42:58	62:38	46:54
n-Dodecane	0	5.8	29.5	48.0	16.6	-	42:58	61:39	45:55
	133.3	5.7	28.7	46.7	18.9	-	42:58	61:39	42:58

[a]: Uncertainty is 0.2 %; [b]: Uncertainty is 0.7 %; [c]: Uncertainty is 0.8 %; [d]: Uncertainty is 0.4 %; [e]: Uncertainty is 0.2 %; [f]: M represents the sum of In and Sn measured.

The as-supplied ITO powder used to fabricate the electrodes in this study was purchased from US Research Nanomaterials, Inc as a 95:5 w/w% mixture of In_2O_3:SnO_2, thus, the atomic ratio of In:Sn was expected to be ~ 95:5. The atomic ratio of In:Sn at the surface of each nITO electrode, as determined by survey XPS (**Figure S14-S17**), was between 82:18 to 84:16, indicating that Sn is preferentially located at the substrate surface. This is consistent with Fan *et al.* who found that tin becomes mobile within the In_2O_3 lattice at elevated temperatures and is thermodynamically favored at interfacial/surface sites rather than interior lattice sites.[29] The greater proportion of Sn at interfacial/surface sites compared to the bulk would suggest that it will be more available for reactions with solvent radiolysis products. Further, the M:O (M = In and Sn) atomic ratio of each electrode was found to be 41:58 or 42:58, which is slightly shifted from that expected for pure stochiometric In_2O_3 (40:60) and corresponds to the presence of oxygen vacancies and other defects in the In_2O_3 lattice caused by Sn-doping and the annealing process. Notably, the measured M:O ratio of nITO electrode surfaces did not exhibit statistically significant changes when soaked or irradiated in any of the solutions.

High-resolution XPS spectra of the In 3d and Sn 3d regions were collected to assess their local environment in soaked and irradiated nITO electrode surfaces (**Figure S6-S9** and **Table S6**). In 3d and Sn 3d spectra were baseline corrected using a Shirley background and fit using methodology established by Donley *et al.* for similar ITO materials.[30] This involved fitting the data using the minimum number of components (70 % Gaussian, 30 % Lorentzian) that provided a reasonably good fit and maintained physical meaning for each element's local environment. The In 3d signal (only $3d_{5/2}$ shown) for each electrode comprised two components at 443.8 ± 0.1 and 444.6 ± 0.1 eV corresponding to signals observed from In_2O_3 and $In(OH)_3$, respectively.[29,30] Similarly, the Sn 3d signal (only $3d_{5/2}$ shown) for each electrode comprised two components at 486.0 ± 0.2 and 486.6 ± 0.2 eV corresponding to Sn substituted into the In_2O_3 lattice, denoted "SnO_2" herein, and $Sn(OH)_x$ species, respectively.[29–31] The ratio of metal oxide to metal hydroxide was lower for Sn compared to In for all samples (**Table *1***). This is likely due to the incorporation of Sn into the In_2O_3 lattice, which correlates with the formation of neighboring point defects that can facilitate the hydrolysis of neighboring metal cations.[30] It may also be attributed to the higher electrophilicity of Sn(IV) compared to In(III). For nITO electrodes soaked or irradiated in each media, similar increases in the In_2O_3:$In(OH)_3$ ratio were observed relative to the pristine electrode, suggesting that interactions with solvent radiolysis products had little effect on In speciation at the nITO substrate surface. The "SnO_2":$Sn(OH)_x$ ratio exhibited solvent and dose dependent shifts, indicating that the speciation of Sn at the surface of the nITO electrode may be more sensitive to changes in solvent conditions and radiation exposure than In.

For nITO electrodes soaked and irradiated in water, the In 3d peak did not change with exposure to gamma radiation, maintaining an In_2O_3:$In(OH)_3$ ratio of 61:39. The speciation of Sn at the nITO electrode

surface experienced a notable shift when exposed to gamma radiation in water, shifting from a "SnO_2":$Sn(OH)_x$ ratio of 47:53 (0 kGy) to 50:50 (100 kGy) (**Figure S7**). A possible mechanism for this behavior involves water radiolysis products, such as $^{\bullet}OH$ (**Reaction 1**), abstracting H-atoms from the hydroxyl groups, specifically Sn-OH, at the ITO surface (**Reaction 6**):[18]

$$Sn\text{-}OH + {}^{\bullet}OH \rightarrow Sn\text{-}O^{\bullet} + H_2O. \quad (6)$$

The resulting metal oxide radicals (Sn-O$^{\bullet}$) may subsequently form Sn=O groups by interacting with other components of the ITO electrode, such as f-center defects. The reaction of $^{\bullet}OH$ with Sn-OH would need to outcompete opposing reactions with reducing radiolysis products, such as H_2O_2, $H^{\bullet}$, and e_{aq}^-, to yield the observed results. Additional studies regarding the reaction rate of these species with ITO, as well as intensive modeling, are needed to identify the kinetically and thermodynamically favored reaction pathway.

For nITO electrodes soaked or irradiated in aqueous 0.1 M HNO_3 solution, radiation exposure predominantly accelerated the dissolution of ITO, as determined by inductively coupled plasma–mass spectrometry (ICP-MS) (**Table S3**). This dissolution resulted in a final nITO surface that resembled that of nITO electrodes irradiated in air. Following irradiation, the relative concentration of C at the nITO surface decreased by 1.7 %, while the relative concentrations of In, Sn, and O increased. The speciation of In and Sn at the nITO electrode surface also changed with exposure to gamma radiation. This exposure resulted in a negligible decrease in the In_2O_3:$In(OH)_3$ ratio from 63:37 to 62:38, and a more significant decrease in the "SnO_2":$Sn(OH)_x$ ratio from 50:50 to 46:54 (**Figure S8**). This shift from M=O to M-OH speciation at the nITO surface is the opposite of what is observed in water. Transitioning from water to aqueous 0.1 M HNO_3 changes the speciation and availability of radiolysis products, which may explain the contradictory nITO surface behavior. In aqueous 0.1 M HNO_3, all the e_{aq}^- are scavenged by NO_3^- (**Reaction 2**) and H_{aq}^+ (pH = 1):

$$H_{aq}^+ + e_{aq}^- \rightarrow H^{\bullet}, \quad (7)$$

with the majority (~70 %) being converted to $H^{\bullet}$ based on reaction kinetics.[18] The resulting increased yield of $H^{\bullet}$ likely leads to more extensive surface adsorption and reduction:

$$Sn{=}O + H^{\bullet} \rightarrow Sn{=}O\cdots H^{\bullet} \rightarrow Sn\text{-}{}^{\bullet}O\text{-}H. \quad (8)$$

Similar reactions between ITO and $H^{\bullet}$ have been observed in high-energy thin-film preparation methods, such as direct-current plasma sputtering, to generate highly reduced ITO substrates, lending precedence to this reaction pathway.[23] A similar argument can be made for the yield of e_{aq}^- (~30 %) being converted into HNO_2 (**Reaction 2**), another molecular reductant. If this is the case, then our observations suggest that the e_{aq}^- does not readily react with surface groups, instead reacting with other components of the solvent or potentially entering the electrode's conduction band.[32] Alternatively, the dissolution of the ITO substrate in aqueous 0.1 M HNO_3 exposes subsurface defects, accumulated from the direct deposition of radiation energy. These exposed species rapidly hydrolyze upon exposure to the solution, favoring the formation of surface hydroxides rather than bridging oxygen groups in this acidic aqueous media.

For nITO electrodes soaked or irradiated in *n*-dodecane, gamma irradiation increased the relative atomic concentration of C by 2.3 %, concomitant with decreases in the relative concentrations of In, Sn, and O. This suggests the addition of various *n*-dodecane radiolysis products (**Reaction 5**) to the nITO surface. This hypothesis is supported by an increase in the 284.6 eV peak in the C 1s signal, indicating a higher relative concentration of CH_x species at the surface (**Figure S5**). The speciation of In at the nITO electrode surface remained unchanged with gamma radiation exposure, maintaining an In_2O_3:$In(OH)_3$ ratio of 61:39 (**Figure S9**). Whereas the speciation of Sn changed with irradiation, resulting in a decrease in the "SnO_2":$Sn(OH)_x$ ratio from 45:55 to 42:58 (**Figure S9**). Xu and coworkers demonstrated that the radical addition of $^{\bullet}CH_3$ to various MO_x substrates was greatly favored when the MO_x was an easily reducible oxide.[33] In this case, Sn(IV) was more easily reduced than In(III),[29,31] suggesting that neutral alkyl radical products from *n*-dodecane radiolysis may preferentially add to surface Sn sites, forming a Sn-O-C linkage (**Reaction 9**):

$$Sn{=}O + {}^{\bullet}CH_2R \rightarrow Sn\text{-}{}^{\bullet}O\text{-}CH_2R. \quad (9)$$

This methoxy-like linkage may manifest in the XPS as Sn 3d and O 1s signal components that overlap with the $Sn(OH)_x$ components.[34,35] Due to ambiguity in assigning peak components and the potential for adventitious sources to interfere with signals, the corresponding O 1s (**Figure S4**) and C 1s (**Figure S5**) spectra were not fit. Additionally, radiation-induced surface defects like oxygen vacancies rapidly react with air or solution molecules, making their detection by *ex situ* measurements unlikely.[27,28] Rather, these spectra were qualitatively compared to determine whether soaking or irradiation caused significant shifts in the local environment of O at the nITO electrode surfaces (**Figure S4**). No notable changes were observed in these spectra.

Overall, these XPS data indicate that the In_2O_3 structure remains intact even when exposed to elevated doses of gamma radiation in each solvent. The speciation of In at the electrode surface showed little change with absorbed gamma dose and varying solvent type, while the speciation of Sn changed more significantly. In water, solvent radiolysis products deprotonated/oxidized Sn sites at the nITO electrode surface, possibly through an H-atom abstraction mechanism. In contrast, the opposite behavior was observed in 0.1 M HNO_3, possibly due to an increased radiolytic yield of $H^{\bullet}$ and HNO_2 that may reduce Sn sites at the nITO electrode surface or due to the accelerated dissolution of the ITO substrate. In *n*-dodecane, solvent radiolysis products were deposited on the nITO electrode surface, suggesting a possible pathway to modify metal oxides with nonpolar alkyl substituents.

3.2. Band Structure

The band structure of metal oxides is often controlled by doping to alter the states that comprise the valence and conduction bands, primarily near the band edges. This includes changing the concentration of a dopant—in this case, Sn in ITO—or the addition of new states through the formation of defects in the material (e.g., oxygen vacancies). Tauc plot analysis (examples shown in **Figure S10**) of UV-vis spectra were used to examine how radiation-induced changes of the nITO surface and subsurface alter the optical bandgap (E_g) of the material. **Figure 3**. and **Table S4** show the relationship between absorbed gamma dose and E_g for each solvent and dose combination. Note that for all irradiated nITO electrodes, regardless of solution conditions, absorbers at energies lower than the material's bandgap were observed (**Figure S1**). This further supports the conclusion that that gamma irradiation of nITO electrodes leads to the formation of defects in the material.

The effect of radiolysis products on the E_g of nITO electrodes was pronounced. After an absorbed dose of 100 kGy (air, water, and aqueous 0.1 M HNO_3) or 133.3 kGy (*n*-dodecane), the E_g of the electrodes irradiated in air, water, and *n*-dodecane decreased by 0.20, 0.19, and 0.27 eV, respectively. This decrease is primarily attributed to the formation of defects in the nITO substrate, which favor bandgap narrowing.[36,37] The bandgap of electrodes irradiated in water narrowed slightly less than those in air, potentially due to the oxidation of the nITO substrate by water radiolysis products (**Reaction 1**). The bandgap in *n*-dodecane narrowed more than those irradiated in air, likely due to the combination of a more reducing environment favoring the increased formation of oxygen vacancies in the nITO film and the deposition of *n*-dodecane radiolysis products to the surface. Contrasting the previous three cases, the E_g of nITO electrodes irradiated in aqueous 0.1 M HNO_3 initially increased by 0.03 eV at an accumulated dose of 25 kGy before decreasing with increasing absorbed dose thereafter. This is likely caused by the combination of nITO dissolution, direct radiolysis effects, and interactions with the more reducing radiolysis products generated in 0.1 M HNO_3, where nITO dissolution and reduction outcompetes radiation-induced defect formation at low dose rates, and the formation of defects becomes more predominant at higher-dose regimes.

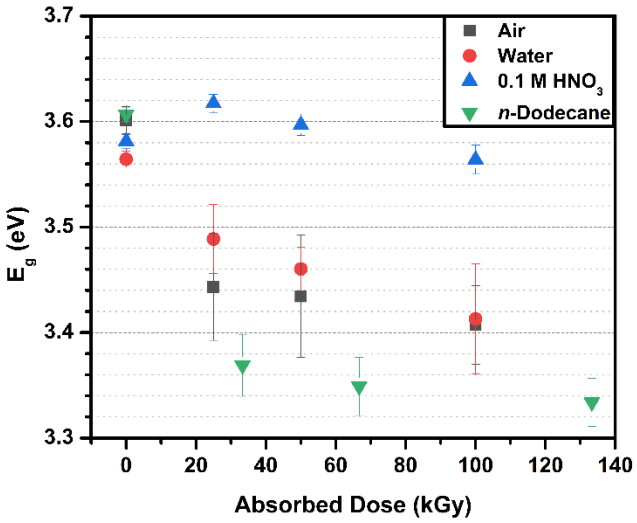

Figure 3. Estimated optical bandgap (E_g) of nITO electrodes as a function of absorbed gamma dose in air (■) or submerged in water (●), aqueous 0.1 M HNO_3 (▲), or *n*-dodecane (▼) solutions. Error bars represent the standard deviation of three bandgap values obtained at three different electrodes for each solvent-dose combination.

To gain more information on how irradiation and solvent radiolysis products alter the band structure of thin film TCOs, the conduction band edge was estimated using a Gärtner–Butler analysis to determine the flat band potential (E_{FB}) of each electrode prepared in this work. For degenerate, highly doped, n-type semiconductors, E_{FB} is approximately equal to the conduction band edge (E_{CB}) of the substrate ($|E_{FB} - E_{CB}| \leq 0.1$ V).[38] These experiments were conducted in the presence of excess H_2O_2 (a well-known hole-scavenger) to ensure the experimentally obtained E_{FB} values were not shifted artificially positive due to factors including slow electron transfer kinetics and large thermodynamic barriers.[39] An example Gärtner–Butler plot of an nITO electrode irradiated in water is shown in **Figure S11**. **Figure 4.** and **Table S5** show that the average experimentally determined flat band potential was shifted as a function of absorbed gamma dose and solvent type. For nITO electrodes irradiated in air, the flat band potential decreased (relative to vacuum) linearly with increasing absorbed dose (-1.3 ± 0.1 meV/kGy), corresponding to a gradual increase in the concentration of defects in the material. The conduction band edge of the ITO consists primarily of In 5*s* orbitals with slight contributions from Sn 5*s* and unoccupied O 2*p* orbitals.[40] The formation of defects not only shift the energies of neighboring In and Sn 5*s* states lower but introduces new states just under the conduction band that result in a lowering of the conduction band edge.[29] Electrodes irradiated in solvents feature deviations in E_{FB} compared to the linear trend observed from those irradiated in air. These deviations are a result of solvent radiolysis product interactions with the TCO material and highlight how the presence of different radiolysis products results in different net effects.

The nITO electrodes irradiated in water display an increase in E_{FB} (relative to vacuum) with increasing absorbed dose, contrary to the trend observed for electrodes irradiated in air. This suggests that water radiolysis products lower the concentration of defect states that contribute to the conduction band edge of nITO, likely through the oxidation of the nITO electrode's surface. These observations underscore the need to perform irradiations under relevant conditions, as the effects of ionizing radiation in the gas phase differ from those in solution.

For electrodes irradiated in aqueous 0.1 M HNO_3 (**Figure 4.**), the relationship between E_{FB} and absorbed gamma dose more closely resembled that of electrodes irradiated in air rather than in water. This supports earlier observations and interpretations that the acid-driven dissolution of the nITO substrate in 0.1 M HNO_3 results in a surface that more accurately reflects the direct effects of radiation. The slight deviations in E_{FB} for nITO electrodes irradiated in 0.1 M HNO_3 compared to those irradiated in air can be

attributed to the combined effects of electrode dissolution, hydrolysis, protonation, and reduction, with dissolution likely being the dominant factor.

The E_{FB} values obtained from electrodes irradiated in *n*-dodecane initially decreased after the first 33.3 kGy (**Figure 4.**), showing a steeper decline than that observed for electrodes irradiated in air. In the subsequent dose range (33.3 to 133.3 kGy), the E_{FB} increased and returned to its original value. The initial decrease suggests that *n*-dodecane radiolysis products such as $H^{\bullet}$, e_S^-, $^{\bullet}CH_3$, and $^{\bullet}CH_2R$ facilitate the formation of defects that lower the conduction band edge. The subsequent increase in E_{FB} from 33.3 to 133.3 kGy likely corresponds to modification of the nITO surface by *n*-dodecane radiolysis product through radical addition reactions. Ligand modification of metal oxide surfaces significantly shifts the observed E_{FB} values; however, the fundamental forces that dictate these observed shifts are not yet well understood. Recent studies have focused on elucidating the fundamental properties that govern the direction and magnitude of band edge shifts due to ligand modification.[41–43] In this case, it appears that modifying nITO materials with nonpolar alkane substituents leads to a positive shift in measured E_{FB} values (relative to vacuum).

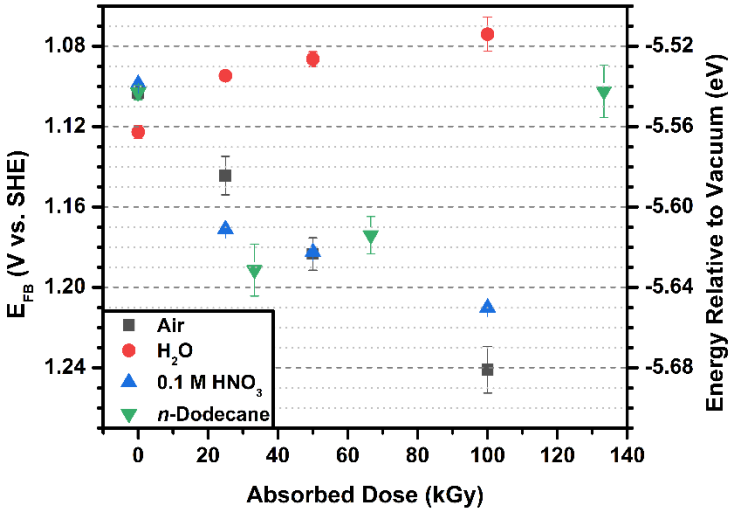

Figure 4. Flat band potentials determined from the Gärtner–Butler method of nITO electrodes as a function of absorbed gamma dose in air (■) or submerged in water (●), aqueous 0.1 M HNO_3 (▲), or *n*-dodecane (▼) solutions. Error bars represent the standard deviation of results obtained at three different light intensities at a single electrode.

These results are significant for band-structure engineering and photochemical applications, as the band narrowing of semiconductors lowers the photon energy required to generate a charge-separated state and the position of the E_{CB} dictates the strength of the available hole. We have shown that gamma irradiation narrows the bandgap of nITO electrodes regardless of the surrounding media, while the E_{CB} may be selectively increased or decreased based on the identity of the surrounding media. A plot of the nITO electrode band structure as a function of solvent and absorbed gamma dose was constructed using the estimated optical E_g and by assuming $E_{FB} \approx E_{CB}$ and is shown in **Figure S12**.

2.3. Electrochemical and Photochemical Performance

The electrochemical performance of unirradiated and irradiated nITO electrodes was determined by cyclic voltammetry of an acetonitrile solution containing 1 mM ferrocene and 0.1 M tetrabutylammonium hexafluorophosphate as a supporting electrolyte. The subtle changes in interfacial composition and changes in band structure from gamma irradiation had no significant impact on the electrochemical performance in

any instance (**Figure 5.**). The capacitive current intrinsic to the nITO electrode was unaffected by increasing dose in each solvent. The current response from the Fe(III/II) redox couple from ferrocene was also unimpacted by the radiation dose each electrode absorbed prior to electrochemical analysis. This includes a minimal change in the peak-to-peak separation ($\Delta\Delta E_{p,Fc} = \pm 24$ mV) and peak current densities ($\Delta i_{p,Fc} = \pm 25$ μA/cm^2) compared to the unirradiated electrode, which suggests that the sum of direct and indirect radiolysis effects in all solvents negligibly impacts the electrochemical performance of nITO electrodes.

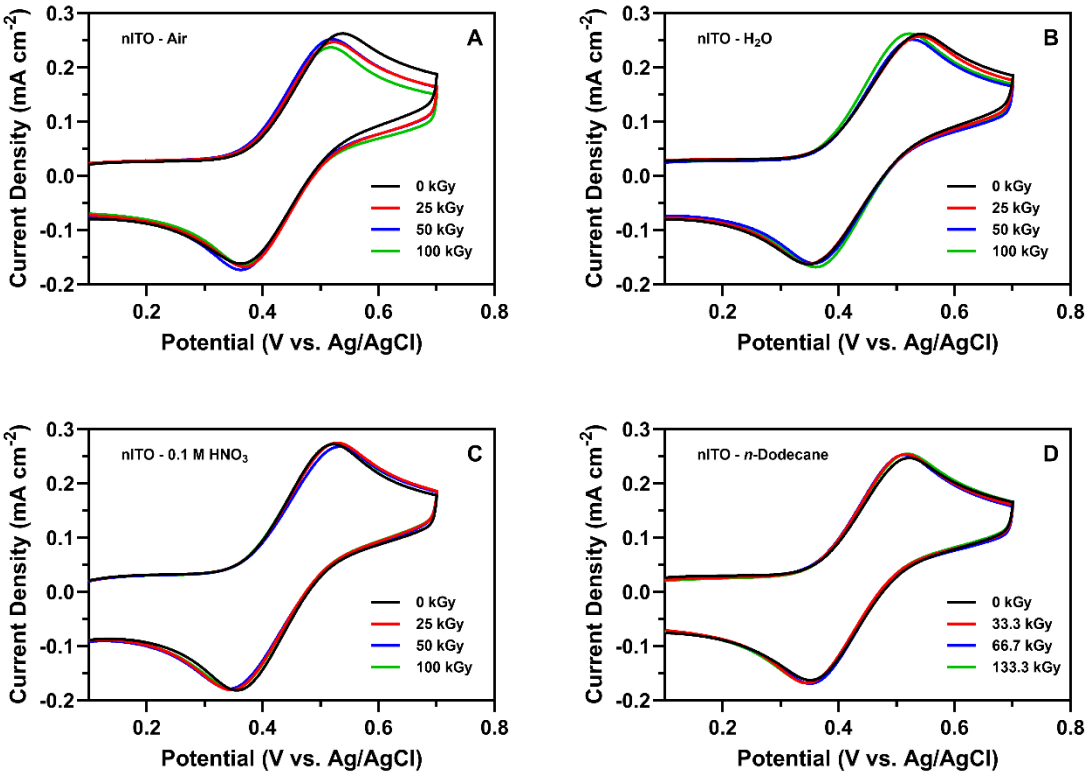

Figure 5. Cyclic voltammograms of an acetonitrile solution containing 1 mM ferrocene and 0.1 M tetrabutylammonium hexafluorophosphate using nITO electrodes either irradiated in air **(A)** or submerged in water **(B)**, aqueous 0.1 M HNO_3 **(C)**, or *n*-dodecane **(D)**. All cyclic voltammograms were acquired at a scan rate of 20 mV/s using a graphite rod counter electrode and Ag/AgCl pseudo-reference electrode.

The photoelectrochemical performance of unirradiated and irradiated nITO electrodes was assessed through the photoelectrochemical oxidation of H_2O_2 in a 0.1 M HNO_3 solution under 375 nm illumination (120 mW/cm^2) (**Figure 6.** and **Figure S13**). For all electrode-solvent combinations, after an absorbed gamma dose of 25 kGy (or 33.3 kGy for *n*-dodecane), the observed photocurrent at 1.3 V *vs.* the saturated calomel electrode (SCE) increased significantly. This increase is attributed to an increase in charge carrier concentration (i.e., oxygen vacancies or other defects) and the introduction of states within the original bandgap of the ITO substrate (i.e., f-centers or other defects). The maximum increase in photocurrent is 68 % for nITO irradiated with a 25 kGy gamma radiation dose in water, while it is a 56 % increase for electrodes irradiated in air, 46 % when irradiated in 0.1 M nitric acid, and only 26 % when irradiated in *n*-dodecane. At accumulated doses above 25 kGy, the photocurrent densities recorded at electrodes irradiated in water and 0.1 M HNO_3 were not significantly altered, while those irradiated in air saw a slight increase in photocurrent from 25 to 50 kGy, and those irradiated in *n*-dodecane saw a slight decrease in photocurrent density from 66.7 to 133.3 kGy. These behaviors correspond to the sum of the radiolytic processes that ultimately affect charge carrier density, recombination rates, and available photoactive sites at the nITO

surface. Additional characterization and modeling are needed to unequivocally identify the mechanisms at play that cause these increases in photocurrents. Overall, the photoelectrochemical performance of nITO electrodes are enhanced while electrochemical performance is preserved within the dose range of 0–100 kGy in air, water, and aqueous 0.1 M HNO_3 and 0–133.3 kGy for *n*-dodecane, indicating that nITO is an ideal photoanode for use within high radiation fields and its performance can be significantly improved by a controlled dose of gamma radiation.

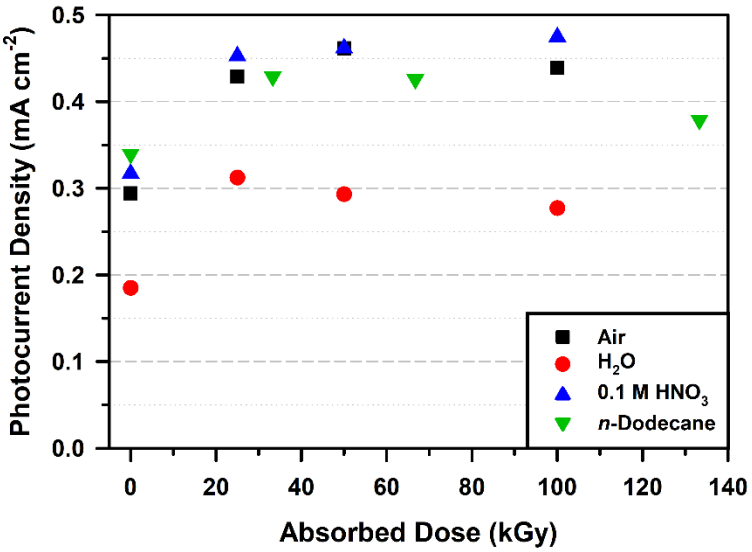

Figure 6. Photocurrent densities at 1.3 V vs. SCE as a function of absorbed gamma dose and solvent type. Photocurrent densities were measured in an aqueous 0.1 M HNO_3 solution containing 0.5 M H_2O_2 at nITO electrodes illuminated with a 120 mW/cm^2 375 nm LED. The counter electrode was a graphite rod, and the measured potentials were referenced against the SCE.

4. Conclusion

Solvent radiolysis products play a subtle yet intricate role in the gamma irradiation of nITO materials. In each solvent, increased absorbed doses of gamma radiation led to the formation of defects, such as oxygen vacancies and f-centers, within the nITO materials. Water radiolysis products were found to preferentially deprotonate and oxidize the nITO substrate, likely resulting in a lower concentration of defects. *n*-Dodecane radiolysis products modified the surface with alkyl groups and likely led to an elevated concentration of defect states. In aqueous 0.1 M HNO_3, changes in the speciation and yields of water radiolysis products led to preferential reduction of the nITO surface, although deeper insights were complicated by concomitant dissolution of the electrodes surface. These interfacial changes altered the band structure of nITO materials, leading to solvent- and dose-specific bandgap narrowing and shifts of the conduction band energy. Finally, irrespective of the solvent, the irradiated nITO materials maintained their utility as electrodes, in addition to their performance as photoanodes increasing. Consequently, nITO electrodes remain an interesting material for application in radiation environments, and further studies with ligand-modified substrates may be beneficial.

5. Supporting Information

The supporting Information consists of a single file that contains information pertaining to ICP-MS, XPS, UV-Vis spectroscopy, pore size distribution, Tauc analysis, Gärtner–Butler analysis, and photoelectrochemical measurements.

6. Acknowledgment

The work of JRM was supported by the U.S. DOE, Office of Science, Office of Workforce Development for Teachers and Scientists, Office of Science Graduate Student Research (SCGSR) program. The SCGSR program is administered by the Oak Ridge Institute for Science and Education for the DOE under contract number DE-SC0014664. GO, XH, and CD as well as electrode development and microscopy was supported by the U.S. Department of Energy (DOE), Office of Science, Office of Basic Energy Sciences, Heavy Element Chemistry program under Award Number DE-SC0023050. GPH, the irradiation work, UV-vis spectroscopy, electrochemical characterization, and ICP-MS studies were supported by the INL Laboratory Directed Research and Development (LDRD) Program under DOE Idaho Operations Office contract DEAC07-05ID14517. SEM images and XPS Spectra were collected at the Chapel Hill Analytical and Nanofabrication Laboratory, CHANL, a member of the North Carolina Research Triangle Nanotechnology Network, RTNN, which is supported by the National Science Foundation, Grant ECCS-1542015, as part of the National Nanotechnology Coordinated Infrastructure, NNCI. We thank Dr. Carrie Donley for her assistance with the XPS spectra and Dr. Amar Kumbhar for acquiring SEM images.

References

(1) Duinong, M.; Chee, F. P.; Salleh, S.; Alias, A.; Salleh, K. A. M.; Ibrahim, S. Structural and Optical Properties of Gamma Irradiated CuGaO2 Thin Film Deposited by Radio Frequency (RF) Sputtering. *J. Phys.: Conf. Ser.* **2019**, *1358* (1), 012047. https://doi.org/10.1088/1742-6596/1358/1/012047.

(2) Paniagua, S. A.; Giordano, A. J.; Smith, O. L.; Barlow, S.; Li, H.; Armstrong, N. R.; Pemberton, J. E.; Brédas, J.-L.; Ginger, D.; Marder, S. R. Phosphonic Acids for Interfacial Engineering of Transparent Conductive Oxides. *Chem. Rev.* **2016**, *116* (12), 7117–7158. https://doi.org/10.1021/acs.chemrev.6b00061.

(3) Cao, W.; Li, J.; Chen, H.; Xue, J. Transparent Electrodes for Organic Optoelectronic Devices: A Review. *JPE* **2014**, *4* (1), 040990. https://doi.org/10.1117/1.JPE.4.040990.

(4) Sheridan, M. V.; McLachlan, J. R.; González-Moya, J. R.; Cortés-Medina, N. D.; Dares, C. J. Indium Tin-Doped Oxide (ITO) as a High Activity Water Oxidation Photoanode. *ACS Appl. Mater. Interfaces* **2021**, *13* (33), 40127–40133. https://doi.org/10.1021/acsami.1c11298.

(5) Fang, Y.; Commandeur, D.; Cheat Lee, W.; Chen, Q. Transparent Conductive Oxides in Photoanodes for Solar Water Oxidation. **2020**. https://doi.org/10.1039/C9NA00700H.

(6) Mustapha, I.; Olarinoye, O.; Ibrahim, S. Transparent Conducting Oxides Thin Film Dosimetry: Present and the Future. *J. Rad. Nucl. Appl.* **2022**, *7* (1), 49–58. https://doi.org/10.18576/jrna/070106.

(7) Alyamani, A.; Mustapha, N. Effects of High Dose Gamma Irradiation on ITO Thin Film Properties. *Thin Solid Films* **2016**, *611*, 27–32. https://doi.org/10.1016/j.tsf.2016.05.022.

(8) Madiba, I. G.; Émond, N.; Chaker, M.; Thema, F. T.; Tadadjeu, S. I.; Muller, U.; Zolliker, P.; Braun, A.; Kotsedi, L.; Maaza, M. Effects of Gamma Irradiations on Reactive Pulsed Laser Deposited Vanadium Dioxide Thin Films. *Applied Surface Science* **2017**, *411*, 271–278. https://doi.org/10.1016/j.apsusc.2017.03.131.

(9) Oryema, B.; Jurua, E.; Madiba, I. G.; Nkosi, M.; Sackey, J.; Maaza, M. Effects of Low-Dose γ-Irradiation on the Structural, Morphological, and Optical Properties of Fluorine-Doped Tin Oxide Thin Films. *Radiation Physics and Chemistry* **2020**, *176*, 109077. https://doi.org/10.1016/j.radphyschem.2020.109077.

(10) Bourezgui, A.; Kacem, I.; Daoudi, M.; Al-Hossainy, A. F. Influence of Gamma-Irradiation on Structural, Optical and Photocatalytic Performance of TiO2 Nanoparticles Under Controlled Atmospheres. *J. Electron. Mater.* **2020**, *49* (3), 1904–1921. https://doi.org/10.1007/s11664-019-07887-z.

(11) Kim, H. J.; Tak, Y. J.; Park, S. P.; Na, J. W.; Kim, Y.; Hong, S.; Kim, P. H.; Kim, G. T.; Kim, B. K.; Kim, H. J. The Self-Activated Radical Doping Effects on the Catalyzed Surface of Amorphous Metal Oxide Films. *Sci Rep* **2017**, *7* (1), 12469. https://doi.org/10.1038/s41598-017-12818-1.

(12) Park, S. J.; Joo, M. H.; Maeng, J. Y.; Rhee, C. K.; Kang, J.-G.; Sohn, Y. Electrochemical Ce3+/Ce4+ and Eu2+/Eu3+ Interconversion, Complexation, and Electrochemical CO2 Reduction on Thio-Terpyridyl-Derivatized Au Electrodes. *Applied Surface Science* **2022**, *576*, 151793. https://doi.org/10.1016/j.apsusc.2021.151793.
(13) Park, S. J.; Joo, M. H.; Yang, J. H.; Hong, S.-M.; Rhee, C. K.; Kang, J.-G.; Sohn, Y. Electrochemical Ce(III)/Ce(IV) Redox Behavior and Ce Oxide Nanostructure Recovery over Thio-Terpyridine-Functionalized Au/Carbon Paper Electrodes. *ACS Appl. Mater. Interfaces* **2021**, *13* (23), 27594–27611. https://doi.org/10.1021/acsami.1c05105.
(14) Hou, X.; McLachlan, J. R.; Dares, C. J. Electrochemical Behaviour of Uranium at a Tripolyphosphate Modified ITO Electrode. *Chem. Commun.* **2021**, *57* (83), 10891–10894. https://doi.org/10.1039/D1CC03877J.
(15) Lopez, M. J.; Sheridan, M. V.; McLachlan, J. R.; Grimes, T. S.; Dares, C. J. Electrochemical Oxidation of Trivalent Americium Using a Dipyrazinylpyridine Modified ITO Electrode. *Chem. Commun.* **2019**, *55* (28), 4035–4038. https://doi.org/10.1039/C9CC00837C.
(16) Dares, C. J.; Lapides, A. M.; Mincher, B. J.; Meyer, T. J. Electrochemical Oxidation of 243Am(III) in Nitric Acid by a Terpyridyl-Derivatized Electrode. *Science* **2015**, *350* (6261), 652–655. https://doi.org/10.1126/science.aac9217.
(17) Spinks, J. W.; Woods, R. J. *An Introduction to Radiation Chemistry*.
(18) Buxton, G. V.; Greenstock, C. L.; Helman, W. P.; Ross, A. B. Critical Review of Rate Constants for Reactions of Hydrated Electrons, Hydrogen Atoms and Hydroxyl Radicals (·OH/·O− in Aqueous Solution. *J. Phys. Chem. Ref. Data* **1988**, *17* (2), 513–886. https://doi.org/10.1063/1.555805.
(19) Katsumura, Y. *The Chemistry of Free Radicals: N-Centered Radicals*; 1998.
(20) Wojnarovits, L.; Schuler, R. H. Bond Rupture in the Radiolysis of N-Alkanes: An Application of Gel Permeation Chromatography to Studies of Radical Scavenging by Iodine. *J. Phys. Chem. A* **2000**, *104* (6), 1346–1358. https://doi.org/10.1021/jp992933r.
(21) Kim, K. Y.; Park, S. B. Preparation and Property Control of Nano-Sized Indium Tin Oxide Particle. *Materials Chemistry and Physics* **2004**, *86* (1), 210–221. https://doi.org/10.1016/j.matchemphys.2004.03.012.
(22) Lee, J.-S.; Choi, S.-C. Solvent Effect on Synthesis of Indium Tin Oxide Nano-Powders by a Solvothermal Process. *Journal of the European Ceramic Society* **2005**, *25* (14), 3307–3314. https://doi.org/10.1016/j.jeurceramsoc.2004.08.022.
(23) Okada, K.; Kohiki, S.; Luo, S.; Sekiba, D.; Ishii, S.; Mitome, M.; Kohno, A.; Tajiri, T.; Shoji, F. Correlation between Resistivity and Oxygen Vacancy of Hydrogen-Doped Indium Tin Oxide Thin Films. *Thin Solid Films* **2011**, *519* (11), 3557–3561. https://doi.org/10.1016/j.tsf.2011.01.249.
(24) de Laharpe, P.; Lin, J.; Peuget, S.; Arena, H.; Taron, M.; Grygiel, C.; Lebius, H.; Deschanels, X. Exploring the Combined Effects of Water Immersion and Ion Irradiation on Mesoporous Silica. *Materials Letters* **2024**, *371*, 136791. https://doi.org/10.1016/j.matlet.2024.136791.
(25) Lou, Y.; Dourdain, S.; Rey, C.; Serruys, Y.; Simeone, D.; Mollard, N.; Deschanels, X. Structure Evolution of Mesoporous Silica under Heavy Ion Irradiations of Intermediate Energies. *Microporous and Mesoporous Materials* **2017**, *251*, 146–154. https://doi.org/10.1016/j.micromeso.2017.05.057.
(26) Lin, J.; Toquer, G.; Grygiel, C.; Dourdain, S.; Guari, Y.; Rey, C.; Causse, J.; Deschanels, X. Behavior of Mesoporous Silica under 2 MeV Electron Beam Irradiation. *Microporous and Mesoporous Materials* **2021**, *328*, 111454. https://doi.org/10.1016/j.micromeso.2021.111454.
(27) Idriss, H. On the Wrong Assignment of the XPS O1s Signal at 531–532 eV Attributed to Oxygen Vacancies in Photo- and Electro-Catalysts for Water Splitting and Other Materials Applications. *Surface Science* **2021**, *712*, 121894. https://doi.org/10.1016/j.susc.2021.121894.
(28) Easton, C. D.; Morgan, D. J. Critical Examination of the Use of X-Ray Photoelectron Spectroscopy (XPS) O 1s to Characterize Oxygen Vacancies in Catalytic Materials and Beyond. *J. Vac. Sci. Technol. A* **2025**, *43* (5), 053205. https://doi.org/10.1116/6.0004686.

(29) Fan, J. C. C.; Goodenough, J. B. X-Ray Photoemission Spectroscopy Studies of Sn-Doped Indium-Oxide Films. *Journal of Applied Physics* **1977**, *48* (8), 3524–3531. https://doi.org/10.1063/1.324149.
(30) Donley, C.; Dunphy, D.; Paine, D.; Carter, C.; Nebesny, K.; Lee, P.; Alloway, D.; Armstrong, N. R. Characterization of Indium−Tin Oxide Interfaces Using X-Ray Photoelectron Spectroscopy and Redox Processes of a Chemisorbed Probe Molecule: Effect of Surface Pretreatment Conditions. *Langmuir* **2002**, *18* (2), 450–457. https://doi.org/10.1021/la011101t.
(31) Ishida, T.; Kobayashi, H.; Nakato, Y. Structures and Properties of Electron-Beam-Evaporated Indium Tin Oxide Films as Studied by x-Ray Photoelectron Spectroscopy and Work-Function Measurements. *Journal of Applied Physics* **1993**, *73* (9), 4344–4350. https://doi.org/10.1063/1.352818.
(32) Zhao, J.; Li, B.; Onda, K.; Feng, M.; Petek, H. Solvated Electrons on Metal Oxide Surfaces. *Chem. Rev.* **2006**, *106* (10), 4402–4427. https://doi.org/10.1021/cr050173c.
(33) Xu, M.; Ballinger, T. H.; Lunsford, J. H. Quantitative Studies of Methyl Radicals Reacting with Metal Oxides. *J. Phys. Chem.* **1995**, *99* (39), 14494–14499. https://doi.org/10.1021/j100039a042.
(34) Matolín, V.; Libra, J.; Škoda, M.; Tsud, N.; Prince, K. C.; Skála, T. Methanol Adsorption on a CeO2(1 1 1)/Cu(1 1 1) Thin Film Model Catalyst. *Surface Science* **2009**, *603* (8), 1087–1092. https://doi.org/10.1016/j.susc.2009.02.010.
(35) Gamba, O.; Hulva, J.; Pavelec, J.; Bliem, R.; Schmid, M.; Diebold, U.; Parkinson, G. S. The Role of Surface Defects in the Adsorption of Methanol on Fe3O4(001). *Top Catal* **2017**, *60* (6–7), 420–430. https://doi.org/10.1007/s11244-016-0713-9.
(36) Gupta, L.; Mansingh, A.; Srivastava, P. K. Band-Gap Narrwing in Tin-Doped Indium Oxide Films. *Applied Surface Science* **1988**, *33–34*, 898–904. https://doi.org/10.1016/0169-4332(88)90396-0.
(37) Ansari, S. A.; Khan, M. M.; Kalathil, S.; Nisar, A.; Lee, J.; Cho, M. H. Oxygen Vacancy Induced Band Gap Narrowing of ZnO Nanostructures by an Electrochemically Active Biofilm. *Nanoscale* **2013**, *5* (19), 9238. https://doi.org/10.1039/c3nr02678g.
(38) Beranek, R. (Photo)Electrochemical Methods for the Determination of the Band Edge Positions of TiO2-Based Nanomaterials. *Advances in Physical Chemistry* **2011**, *2011* (1), 786759. https://doi.org/10.1155/2011/786759.
(39) Hankin, A.; Bedoya-Lora, F. E.; Alexander, J. C.; Regoutz, A.; Kelsall, G. H. Flat Band Potential Determination: Avoiding the Pitfalls. *J. Mater. Chem. A* **2019**, *7* (45), 26162–26176. https://doi.org/10.1039/C9TA09569A.
(40) Walsh, A.; Catlow, C. R. A. Structure, Stability and Work Functions of the Low Index Surfaces of Pure Indium Oxide and Sn-Doped Indium Oxide (ITO) from Density Functional Theory. *J. Mater. Chem.* **2010**, *20* (46), 10438–10444. https://doi.org/10.1039/C0JM01816C.
(41) Lee, M. G.; Jin, K.; Kwon, K. C.; Sohn, W.; Park, H.; Choi, K. S.; Go, Y. K.; Seo, H.; Hong, J. S.; Nam, K. T.; Jang, H. W. Efficient Water Splitting Cascade Photoanodes with Ligand-Engineered MnO Cocatalysts. *Advanced Science* **2018**, *5* (10), 1800727. https://doi.org/10.1002/advs.201800727.
(42) Kroupa, D. M.; Vörös, M.; Brawand, N. P.; McNichols, B. W.; Miller, E. M.; Gu, J.; Nozik, A. J.; Sellinger, A.; Galli, G.; Beard, M. C. Tuning Colloidal Quantum Dot Band Edge Positions through Solution-Phase Surface Chemistry Modification. *Nat Commun* **2017**, *8* (1), 15257. https://doi.org/10.1038/ncomms15257.
(43) Brown, P. R.; Kim, D.; Lunt, R. R.; Zhao, N.; Bawendi, M. G.; Grossman, J. C.; Bulović, V. Energy Level Modification in Lead Sulfide Quantum Dot Thin Films through Ligand Exchange. *ACS Nano* **2014**, *8* (6), 5863–5872. https://doi.org/10.1021/nn500897c.
(44) Farnum, B. H.; Wee, K.-R.; Meyer, T. J. Self-Assembled Molecular p/n Junctions for Applications in Dye-Sensitized Solar Energy Conversion. *Nature Chem* **2016**, *8* (9), 845–852. https://doi.org/10.1038/nchem.2536.
(45) Horne, G. P.; Zalupski, P. R.; Daubaras, D. L.; Rae, C.; Mezyk, S. P.; Mincher, B. J. Radiolytic Degradation of Formic Acid and Formate in Aqueous Solution: Modeling the Final Stages of

Organic Mineralization under Advanced Oxidation Process Conditions. *Water Research* **2020**, *186*, 116314. https://doi.org/10.1016/j.watres.2020.116314.
(46) Fricke, H.; Hart, E. J. The Oxidation of Fe++ to Fe+++ by the Irradiation with X-Rays of Solutions of Ferrous Sulfate in Sulfuric Acid. *J. Chem. Phys.* **1935**, *3* (1), 60–61. https://doi.org/10.1063/1.1749558.
(47) Tauc, J.; Grigorovici, R.; Vancu, A. Optical Properties and Electronic Structure of Amorphous Germanium. *Physica Status Solidi (b)* **1966**, *15* (2), 627–637. https://doi.org/10.1002/pssb.19660150224.
(48) Davis, E. A.; Mott, N. F. Conduction in Non-Crystalline Systems V. Conductivity, Optical Absorption and Photoconductivity in Amorphous Semiconductors. *Philosophical Magazine* **1970**, *22* (179), 0903–0922. https://doi.org/10.1080/14786437008221061.
(49) Makuła, P.; Pacia, M.; Macyk, W. How To Correctly Determine the Band Gap Energy of Modified Semiconductor Photocatalysts Based on UV–Vis Spectra. *J. Phys. Chem. Lett.* **2018**, *9* (23), 6814–6817. https://doi.org/10.1021/acs.jpclett.8b02892.

Table of Contents Graphic